Preclinical evaluation of [^{11}C]CHDI-009R for quantification of mutant huntingtin aggregates

Authors

Franziska Zajicek[1,2], Liesbeth Everix[1,2], Annemie Van Eetveldt[1,2], Jeroen Verhaeghe[1,2], Stef De Lombaerde[1,3], Alan Miranda[1,2], Jordy Akkermans[1,2], Celia Dominguez[4], Vinod Khetarpal[4], Jonathan Bard[4], Longbin Liu[4], Steven Staelens[1,2], Daniele Bertoglio[2,5]

[1]Molecular Imaging Center Antwerp (MICA), University of Antwerp, Antwerp, Belgium

[2]μNeuro Research Center of Excellence, University of Antwerp, Antwerp, Belgium

[3]Department of Nuclear Medicine, Antwerp University Hospital, Antwerp, Belgium

[4]CHDI Management, Inc., the company that manages the scientific activities of CHDI Foundation, Inc., Los Angeles, CA, USA

[5]Bio-Imaging Lab, University of Antwerp, Antwerp, Belgium

Corresponding author:

Dr. Daniele Bertoglio

Bio-Imaging Lab, Faculty of Pharmaceutical, Biomedical and Veterinary Sciences,

University of Antwerp, Universiteitsplein 1, Wilrijk, Belgium

Tel. +32 3 265 8736

Email: daniele.bertoglio@uantwerpen.be

ORCID

Franziska Zajicek: 0000-0001-5410-687X

Liesbeth Everix: 0000-0001-5985-1609

Annemie Van Eetveldt: 0000-0002-6488-5456

Jeroen Verhaeghe: 0000-0002-4493-1902

Stef De Lombaerde: 0000-0002-5307-3575

Alan Miranda: 0000-0002-5381-015X
Jordy Akkermans: 0000-0002-1533-9504
Vinod Khetarpal: 0000-0002-2175-5117
Jonathan Bard: 0000-0002-5097-1361
Longbin Liu: 0000-0003-3995-0196
Steven Staelens: 0000-0003-3376-0519
Daniele Bertoglio: 0000-0003-4205-5432

Keywords

Positron Emission Tomography; Huntington's disease; kinetic modeling; mHTT aggregates; [^{11}C]CHDI-009R; zQ175DN

Abstract

Huntington's disease (HD) is a neurodegenerative disorder caused by an expanded trinucleotide repeat in the huntingtin gene (*HTT*) that subsequently leads to aggregation of the mutant huntingtin (mHTT) protein. Thus, lowering mHTT is a key therapeutic approach used by several candidate therapeutics currently under investigation. Visualization of the efficiency of these therapeutics through *in vivo* mHTT quantification rises in importance. For positron emission tomography (PET) imaging of mHTT aggregates, it is critical to characterize the *in vivo* kinetic profile of newly identified mHTT binders to assess their translational application. Here, we report the evaluation of [^{11}C]CHDI-009R, a PET imaging radioligand with higher affinity and selectivity for mHTT aggregates than previously reported radioligands, in the heterozygous (HET) zQ175DN mouse model of HD wild-type (WT) littermates at 9 and 3 months of age.

[^{11}C]CHDI-009R displayed high stability in plasma and brain, which was reflected in brain kinetics as demonstrated by rapid uptake followed by relatively slow elimination. Kinetic modeling and volume of distribution $V_{T\ (IDIF)}$ indicated the radioligand's ability to quantify mHTT aggregation at 9 months of age with clear genotype differentiation ($p<0.0001$). [^{11}C]CHDI-009R showed an excellent test-retest reliability in 9-month-old mice (intraclass correlation coefficient: 0.62 - 0.79). A phenotypic difference in mHTT aggregates was also observed in 3-month-old mice in several brain structures ($p<0.05$) and was confirmed with [^{3}H]CHDI-009R autoradiography.

Overall, this study suggests [^{11}C]CHDI-009R is a promising radioligand for the detection of cerebral mHTT aggregates in a mouse model of HD and supports its advance to clinical evaluation.

Introduction

Huntington's disease (HD) is a progressive neurodegenerative disorder caused by an expanded trinucleotide (CAG) repeat in exon 1 of the huntingtin (*HTT*) gene. The transcription and translation of mutant *HTT* leads to the aggregation of mutant huntingtin (mHTT) protein [1, 2], which, alongside mHTT fragments, is involved in cellular dysfunction and loss of neurons [3, 4]. With several disease-modifying therapeutic interventions aimed to lower mHTT expression under clinical investigation [5-7] (e.g. ClinicalTrials.gov identifier (ID): NCT06024265; NCT05032196), there is an increasing interest in accurately quantifying their ameliorative effect. Currently, the estimate of the central nervous system (CNS) target engagement of HTT-lowering therapeutics is indirect, relying on extrapolations of soluble HTT levels in non-brain compartments, such as cerebrospinal fluid, both in the preclinical [8] and clinical setting [9] (www.clinicaltrials.gov, identifier NCT02519036). In this context, positron emission tomography (PET) imaging of mHTT aggregates holds great potential for non-invasive and longitudinal measurement of CNS target engagement at a brain region-specific level, as previously demonstrated [10]. Thus, enabling accurate spatial and temporal evaluation of efficacy with potential therapeutic interventions.

We recently described a number of novel radiotracers for mHTT aggregate imaging in preclinical imaging studies, namely [^{11}C]CHDI-626 [11-13], [^{11}C]CHDI-180R [10, 12, 14, 15] and [^{18}F]CHDI-650 [16, 17] with varying levels of applicability in mice. Additionally, [^{11}C]CHDI-626 [18] and [^{11}C]CHDI-180R [19] were advanced to the clinic but were later discontinued due to either an undesirable brain uptake and decay profile ([^{11}C]CHDI-626) or inability to show a significant difference between people with HD (PwHD) and healthy controls ([^{11}C]CHDI-180R). Thus, until a clinical candidate proves successful in mouse models of HD and PwHD, the identification of novel radioligands targeting mHTT aggregates with superior PET radiotracer properties remains a priority. Especially regarding clinical importance, enhanced sensitivity of mHTT aggregate detection in 3-month-old zQ175DN HET mice is desired as mHTT aggregation is expected to be lower in abundance in humans than in mouse models.

92 Therefore, we report here on the investigation of a novel radioligand, [^{11}C]CHDI-009R, that
93 has been shown to have an almost 3-fold higher maximum specific binding than CHDI-180R
94 ([^{3}H]CHDI-009R: B_{max}=448 fmol/mg; [^{3}H]CHDI-180: B_{max}=163 fmol/mg) in homozygous (HOM)
95 zQ175DN brains (*Liu et al., under review*). We characterize the *in vivo* performance of this
96 tracer in WT and HET zQ175DN knock-in mice through radiometabolite analysis, test-retest
97 variability estimation, quantitative phenotypic comparison at two different ages, and
98 autoradiography with [^{3}H]CHDI-009R.
99

100 # Methods

101 ## Animals

102 A total of 72 nine-month-old male HET (*n*=36) and WT (*n*=36) as well as 48 three-month-old
103 male HET (*n*=24) and WT (*n*=24) zQ175DN mice (B6.129S1-*Htt*$^{tm1.1Mfc}$/190ChdiJ JAX stock
104 #029928), were obtained from Jackson Laboratories (Bar Harbour, Maine, USA) [20, 21]. Due
105 to sporadic congenital portosystemic shunt occurring in C57BL/6J mice [22], all animals were
106 screened at Jackson Laboratories before shipment and hence, all animals used in this study
107 were shunt-free. Study design, group size, body weight, and age of the animals are reported
108 in supplementary Fig. S1, Tables S1-S3. Animals were single-housed at 9 months of age and
109 group-housed at 3 months of age in ventilated cages under a 12 h light/dark cycle. The animals
110 were kept in a temperature- and humidity-controlled environment with food and water *ad*
111 *libitum*. The animals were given at least one week for acclimatization after arrival before the
112 start of any procedure. Experiments followed the European Committee (decree 2010/63/CEE)
113 and were approved by the Ethical Committee for Animal Testing (ECD 2019-39) at the
114 University of Antwerp (Belgium).

115

116 ## Radioligand synthesis

117 [^{11}C]CHDI-009R was prepared using an automated synthesis module (Carbonsynthon I,
118 Comecer, The Netherlands). The radioligand was prepared via single-step carbon-11 labeling
119 at the pyridazinone-NH site, starting with a solution of the precursor (0.3 mg) in DMF (0.5 ml),
120 which was reacted with excess of [^{11}C]CH_3OTf in the presence of NaOH (1 M, 5 µl) for 3 min
121 at room temperature. To terminate the reaction and to ensure good retention of the compound
122 of interest on the semi-preparative HPLC column, acetonitrile/water (35:65, v/v, 2 ml) was
123 introduced to the reaction mixture, and the resulting crude product was purified on HPLC using
124 an ACE 5 C18-HL 250x10 mm column (ACE, UK), eluted with a mixture of ammonium formate
125 (0.1 M) in acetonitrile (35/65, v/v) as mobile phase, at a flow rate of 6 ml/min. The collected
126 fraction was diluted with water (20 ml) before being loaded on a 1 cc 10 mg Oasis HLB

127 cartridge (Waters, MA, USA). The cartridge was washed with water for injection (3 ml) and
128 eluted through a sterile filter with ethanol (0.5 ml) and saline (4.5 ml) to afford the final product
129 solution.
130 The radiochemical purity of the produced [^{11}C]CHDI-009R was determined using a Kinetex
131 EVO C18, 5µm, 150×4.6 mm (Phenomenex, USA) HPLC column, with a solution of sodium
132 acetate (NaOAc) (0.05 M, pH 5.5) in acetonitrile/ (30:70, v/v) as mobile phase, at a flow of 1
133 ml/min, with UV absorbance set at 289 nm. Based on 37 productions, radiochemical purity
134 was greater than 99%, a molar activity (A_M) of 93.59±27.61 GBq/µmol, and a radiochemical
135 yield of 7.83±0.03% was achieved.
136

137 **Radiometabolite analysis**

138 Evaluation of *in vivo* plasma and brain radiometabolite profiles was performed at 5, 20, and
139 40 min post-injection (p.i.). Mice were injected via the lateral tail vein with [^{11}C]CHDI-009R
140 (WT: 3.78±0.87 MBq; HET: 3.75±0.62 MBq in 200 µl), and blood was withdrawn via cardiac
141 puncture at designated times, and brains were immediately excised. The homogenization and
142 extraction were conducted as previously described [10, 17]. The extraction efficiency from
143 plasma samples (percentage of recovery of radioactivity) was 98.4±2.6%, whereas in brain
144 samples, an extraction efficiency of 100.6±4.7% was achieved. Plasma or brain supernatant
145 was loaded onto a pre-conditioned reverse-phase (RP)-HPLC system (Luna C18(2), 5 µm
146 HPLC column (250x4.6 mm) + Phenomenex security guard pre-column) and eluted with
147 NaOAc 0.05M pH 5.5 and acetonitrile: (87:13 for 10 min v/v) buffer at a flow rate of 1 ml/min.
148 RP-HPLC fractions were collected at 0.5 min intervals for 10 min. Pure tracer (5µCi) was
149 loaded onto the same HPLC setup (Fig. S2). Control experiments confirmed that no apparent
150 degradation of the radiotracer occurred during procedural work-up in both plasma
151 (99.91±0.00% of intact tracer) and brain (92.14±0.07% of intact tracer).
152

153 **Dynamic PET imaging acquisition**

154 Dynamic microPET/Computed tomography (CT) images were acquired on Siemens Inveon
155 PET-CT scanners (Siemens Preclinical Solution, Knoxville, USA). Animal preparation was
156 performed as previously described [10, 23]. Animal and dosing information for both WT and
157 HET mice of all paradigms are given in the supplementary Tables S1-S3.
158 PET data were acquired in list mode format. Following the microPET scan, a 10 min 80 kV/500
159 μA CT scan was performed for attenuation and scatter correction. The same microPET scan,
160 was also used to estimate the blood radioactivity through a non-invasive image-derived input
161 function (IDIF) to estimate the volume of distribution ($V_{T\ (IDIF)}$) as a surrogate of V_T.
162 Acquired PET data were reconstructed into 39 frames of increasing length (12x10s, 3x20s,
163 3x30s, 3x60s, 3x150s, and 15x300s). Images were reconstructed using a list-mode iterative
164 reconstruction proprietary spatially variant resolution modeling in 8 iterations and 16 subsets
165 of the 3D ordered subset expectation maximization (OSEM 3D) algorithm [24]. Normalization,
166 dead time, and CT-based attenuation corrections were applied, and PET image frames were
167 reconstructed on a 128x128x159 grid with 0.776x0.776x0.796 mm^3 voxels.
168

169 **Image processing and analysis**

170 Image processing and analysis were performed with PMOD 3.6 software (PMOD
171 Technologies, Zurich, Switzerland) as previously described [11]. For spatial normalization of
172 the PET/CT images, brain normalization of the CT image to a CT template was performed by
173 adapting the previously described protocol [25]. We applied the volumes-of-interests (VOIs)
174 described in previous studies [10, 11], adapted from the Waxholm atlas [26]. Using those VOIs,
175 time activity curves (TACs) were then extracted for individual brain regions. The IDIFs were
176 extracted from the PET images by generating a VOI in the lumen of the left ventricle at an
177 early time frame exhibiting maximal activity in the heart and applying a threshold of 50% of the
178 max signal as previously described [23, 27-29]. Standardized uptake value (SUV) was
179 calculated as activity concentration [kBq/cc] divided by injected dose [kBq] per body weight
180 [g].

181 These regional TACs and IDIFs were used to estimate $V_{T\ (IDIF)}$ values through kinetic modeling.
182 $V_{T\ (IDIF)}$ was estimated by fitting the extracted TACs with standard two-tissue compartmental
183 model (2TCM), with blood volume fraction (V_B) fixed at 3.6% [10, 11] and Logan linear model
184 to calculate $V_{T\ (IDIF)}$. Pixelwise kinetic modeling was performed using the Logan graphical
185 analysis in PXMOD (PMOD 4.2). The averaged parametric maps were subsequently overlaid
186 onto a Waxholm MRI template.
187

188 **Tissue collection for Autoradiography**

189 Animals were euthanized by decapitation while under anaesthesia. Brains were dissected and
190 fresh-frozen in 2-metylbuthane at − 35°C for 2 min and preserved at −80°C. Coronal sections
191 of 10 µm thickness were collected at 1.10 mm from the bregma according to Paxinos and
192 Franklin [30] in triplicate using a cryostat (Leica, Germany) on Superfrost Plus slides (Thermo
193 Fischer Scientific, USA).
194

195 **Autoradiography**

196 [^{3}H]CHDI-009R was provided by Novandi Chemistry AB (Sweden) with a A_M of 82 Ci/mmol.
197 Sections were air-dried at room temperature, pre-incubated for 20 min with binding buffer
198 (50mM Tris-HCl + 120mM NaCl + 5mM KCl + 2mM $CaCl_2$ + 1mM $MgCl_2$, pH 7,4) and air-dried
199 using warm airflow. Dried sections were subsequently incubated with total binding solution
200 (TB, 0.5 nM of [^{3}H]CHDI-009R in binding buffer), non-specific binding solution (NSB, 0.5 nM
201 of [^{3}H]CHDI-009R + 10 µM of cold ligand in binding buffer) was performed for 1h at room
202 temperature. Subsequently, sections were washed three times for 10 min in ice cold washing
203 buffer (50mM Tris-HCl, pH 7,4), followed by a brief wash in ice cold distilled water, and dried
204 for 2h at room temperature. Finally, all sections were exposed on imaging plates (BAS-
205 TR2025, Fujifilm, Japan) for 120 min. Radioactivity was detected with a phosphor imager (Fuji
206 FLA-7000 image reader) and quantified based on intensity values calculated using
207 commercial tritium standards (American Radiolabelled Chemicals Inc., USA). For all samples,

208 the entire surface of the coronal brain slice was used for quantification. The specific binding
209 was determined by subtracting NSB from TB, which were both measured in triplicate and
210 subsequently averaged. The specific binding averages were used for statistical analysis.
211 Specific binding was set to 0 if the values of NSB and TB were below the limit of detectability
212 of the calibration curve. Analysis was performed blind to conditions in Fiji, ImageJ (National
213 Institute of Health, USA, version: 2.1).
214

215 **Statistical analysis**

216 The Shapiro-Wilk test revealed that *in vivo* data were normally distributed, while *in vitro* data
217 demonstrated a non-gaussian distribution; therefore, non-parametric testing was performed
218 on *in vitro* data. All data was visually inspected for outliers followed, if necessary, by statistical
219 outlier testing with ROUT (Q=0.5%). Two outliers in motor cortex for 9-month-old HET mice
220 were identified and excluded. A Pearson's correlation with simple linear regression was
221 applied to $V_{T\,(IDIF)}$ values from 2TCM and Logan kinetic modeling for model verification. A
222 Spearman's correlation with interpolation (sigmoidal, 4PL, X is concentration) was applied to
223 injected masses and $V_{T\,(IDIF)}$ values from Logan for visualization of a potential mass dose
224 effect. Regular two-way ANOVA with *post-hoc* Bonferroni correction for multiple comparisons
225 was applied to analyze $V_{T\,(IDIF)}$ value differences between genotypes.
226 The individual relative test-retest variability (rTRV) was calculated as follows:

227 $$\frac{test - retest}{average\ (test, retest)}$$

228 The individual absolute test-retest variability (aTRV) was calculated as follows:

229 $$\left|\frac{test - retest}{average\ (test, retest)}\right|$$

230 In addition, a Bland-Altman analysis was performed to assess the agreement between two
231 measures on an individual level. A Mann-Whitney test was performed to investigate
232 phenotypic differences in specific binding in autoradiography.

All statistical analyses above were performed with GraphPad Prism (version 9.2.0) statistical software. The Intraclass correlation coefficient (ICC) for the test-retest variability study was calculated with the software JMP Pro 17 (v17.0.0). Group and timepoint interaction was set as fixed effect. Animal ID, timepoint, interaction of animal ID and group, and interaction of animal ID and timepoint, were set as random effects. No effect was identified for either interaction. The ICC was reported as the ratio of the animal variance component for the effect to the sum of positive variance components. One-tailed power analyses were performed in G*Power (v3.1.9.6) with significance level (α) at 0.05, confidence (β) set to 80%. Data are represented as mean ± standard deviation (SD) or as mean ± standard error of the mean (SEM). All tests were two-tailed unless stated otherwise. Statistical significance was set at $p<0.05$ with the following standard abbreviations used to reference p values: ns, not significant; *$p<0.05$; **$p<0.01$; ***$p<0.001$; ****$p<0.0001$.

246 # Results

247 **[^{11}C]CHDI-009R demonstrates high metabolic stability**

248 [^{11}C]CHDI-009R plasma analysis revealed a high stability over time in both plasma (e.g. 40
249 min: WT=95.1±1.7%; HET=96.4±1.2%; Fig. 1a) and brain (e.g. 40 min: WT=90.9±8.6%;
250 HET=93.8±2.0%; Fig. S2) with no observable peak other than the intact ligand (Fig. S2). In
251 addition, the plasma-to-whole-blood ratio was stable over time with no difference observed
252 between genotypes (WT=1.8±0.1; HET=1.7±0.2; Fig. 1b). IDIF profiles of both genotypes
253 displayed a comparable peak within 2 min of radioligand injection and a similar stable signal
254 after 5 min p.i. until the end of acquisition (Fig. 1c). Given the high stability and no difference
255 between genotypes, no corrections were applied to IDIFs for accurate $V_{T\ (IDIF)}$ estimations.

256

257 **[^{11}C]CHDI-009R kinetic modeling with 90 min scan duration**

258 The averaged striatal SUV TACs of [^{11}C]CHDI-009R demonstrated rapid penetration into the
259 brain in both genotypes, but a subsequent slower wash-out was observed in the brain in HET
260 animals compared to WTs (Fig. 2a). We further observed an excellent agreement between
261 2TCM quantification and Logan graphical analysis (striatum: r^2=0.996; p<0.0001) with minimal
262 deviation from the identity line (slope = 0.998) (Fig. 2b); thus, supporting the use of Logan
263 graphical analysis to quantify [^{11}C]CHDI-009R in mice.

264 Next, we performed a $V_{T\ (IDIF)}$ time stability analysis to estimate the shortest recommmended
265 acquisition time. Although we observed no impact on $V_{T\ (IDIF)}$ in WT animals (Fig. 2c), $V_{T\ (IDIF)}$
266 in HET mice was susceptible to a steady underestimation, which passed the 90% threshold
267 with a 60 min acquisition (Fig. 2d). Thus, shortening the scan acquisition time from 90 min
268 was not recommended to avoid even minimal underestimation of a phenotypic effect. Further,
269 we investigated the impact of injected mass on [^{11}C]CHDI-009R $V_{T\ (IDIF)}$. As shown in Fig. S3,
270 a definite negative association was observed; thus, the recommended upper limit for injectable
271 mass was set to 1.7 µg/kg.

272

273 **[^{11}C]CHDI-009R quantification reveals phenotypic differences**

274 The averaged parametric $V_{T\ (IDIF)}$ maps of WT and HET mice shown in Fig. 3a visualize a clear
275 genotype effect. The two-way ANOVA test revealed a significant genotype effect ($F_{(1,\ 183)}$ =
276 987.3; p<0.0001) and the Bonferroni post-hoc analysis demonstrated statistically significant
277 increased signal in HET mice compared to their WT littermates in all tested brain regions
278 (p<0.0001) (Fig. 3b). Phenotypic $V_{T\ (IDIF)}$ differences ranged from 55.5±5.4% in the cerebellum
279 to 105.8±6.2% in the thalamus (Table 1).

280

281 **[^{11}C]CHDI-009R displayed excellent test-retest reproducibility**

282 To measure the reliability of [^{11}C]CHDI-009R, a test-retest study was performed in WT and
283 HET zQ175DN mice at 9 months. Parametric $V_{T\ (IDIF)}$ maps did not reveal any apparent
284 differences between scans (Fig. 4a). The aTRV was overall low, indicating a high reliability,
285 with a range from 5.1±4.0% to 7.7±4.2% in striatum of WT and HET animals (Fig. 4b; Table
286 2). The Bland-Altmann plot displayed close-ranged levels of agreement (-16.0% to 14.7%)
287 (Fig. 4c). In addition, the regional rTRV, with values ranging from -3.1±8.5% to 4.3±8.3% in
288 WT and from -4.8±6.2% to 1.2±8.3% in HET, demonstrated limited difference across brain
289 regions (Table 2). Overall, according to the ICC values, [^{11}C]CHDI-009R displayed a good to
290 excellent test-retest agreement (Table 2).

291

292 **[^{11}C]CHDI-009R differentiated genotypes at 3 months**

293 In addition to the comprehensive assessment of [^{11}C]CHDI-009R properties at 9 months, a
294 study was performed at 3 months, when less mHTT aggregates are present in HET zQ175DN
295 mice, providing insights into the degree of sensitivity for this radioligand. Based on parametric
296 $V_{T\ (IDIF)}$ maps, an increased signal in HET mice could be detected (Fig. 5a). Accordingly, the
297 two-way ANOVA test revealed a significant genotype effect ($F_{(1,\ 175)}$ = 62.3; p<0.0001). The
298 Bonferroni post-hoc analysis displayed statistically significant phenotypic differences between
299 genotypes, ranging from 8.3±2.7% to 16.3±2.9% in test regions, with the exception of motor
300 cortex (5.0±2.8%; not significant) (Fig. 5b; Table 3). The mHTT aggregate binding capacity of

301 CHDI-009R was also demonstrated through a post-mortem autoradiography study with the
302 tritiated version of the ligand. [^{3}H]CHDI-009R displayed a significantly different specific binding
303 in HET mice compared to WT littermates (Fig. 5c, $p<0.0001$).
304
305 **[^{11}C]CHDI-009R is suitable for evaluating therapeutic efficacy in zQ175DN mice**
306 We performed power analyses to estimate group sizes needed for evaluating therapeutic
307 efficacy (α=0.05, β=80%) in zQ175DN mice. As shown in Table S4, statistical power was
308 good, as revealed by the range of Cohen's *d* of 0.59 – 1.70 and 3.52 – 5.15 at 3 and 9 months,
309 respectively. This indicated that at 9 months, [^{11}C]CHDI-009R could significantly display a 20%
310 difference in mHTT aggregates with acceptable group arms (e.g. striatum: n=21). At 3 months,
311 however, only in striatum (n=23) and thalamus (n=26) could a larger effect (50% difference)
312 between groups be detected with a similar sample size.
313

314 ## Discussion

315 Here we report the *in vivo* characterization of a novel mHTT aggregate PET radioligand,
316 [^{11}C]CHDI-009R, with higher selectivity (*Liu et al., under review*) than previously investigated
317 radiotracers [12, 15, 16]. We show that [^{11}C]CHDI-009R rapidly enters the brain followed by
318 wash-out, indicating its reversible binding. The slower rate of radioligand wash-out from the
319 brain of the HET animals was likely due to the presence of mHTT aggregates that are absent
320 in WT. [^{11}C]CHDI-009R demonstrated high stability in mouse plasma, and no metabolite
321 correction was deemed necessary for IDIFs, although we could only obtain data until 40 min
322 p.i. due to the loss of radioactive signal at later time points in the limited blood sample that can
323 be collected as a consequence of the radioisotope's half-life.

324 The cerebral retention time for both genotypes was suitable for estimating the $V_{T\ (IDIF)}$, for which
325 both 2TCM and Logan graphical analysis was shown as adequate models. The time stability
326 kinetic analysis revealed that a reduction in scan acquisition time was not feasible without
327 introducing a genotype-specific underestimation of the $V_{T\ (IDIF)}$ values, which would result in an
328 artificial decrease of phenotypic differences. The current scan duration of 90 min, however,
329 borders the capability of obtaining data with limited noise due to the short half-life of the isotope
330 (20.4 min), which requires a prompt scan acquisition and keeping the injected mass within the
331 recommended limit of 1.7 µg/kg.

332 With those optimized PET imaging conditions, quantification with Logan indicated that
333 [^{11}C]CHDI-009R could significantly distinguish genotypes at both 9 and 3 months of age, with
334 comparable magnitude as observed with previous mHTT radiotracers [10, 17]. Noteworthy,
335 there was no change in $V_{T\ (IDIF)}$ values of WT animals across brain regions, indicating that
336 [^{11}C]CHDI-009R can reliably and uniformily show the lack of a target in WT animals. Moreover,
337 the post-mortem [^{3}H]CHDI-009R autoradiography confirmed the lack of mHTT aggregates in
338 WT mice, corroborating the previously described findings (*Liu et al., under review*). This
339 represents an important indication of minimum off-target binding that could otherwise

340 potentially diminish the utility of a radioligand, as shown for several Alzheimer's disease-
341 related radioligands [31].
342 Besides general affinity and selectivity, intra-subject variability was also an important factor to
343 be considered. The reliability of [^{11}C]CHDI-009R was demonstrated by the excellent test-retest
344 performance as determined via Bland-Altman plot and ICC values [32]. This provides a
345 significant benefit for a more accurate application, especially in longitudinal settings, and
346 represents a favorable attribute compared to the poor reliability of [^{18}F]CHDI-650 (ICC: 0.00 –
347 0.27) [17].
348 The capability of detecting early changes at the molecular level represents another important
349 utility in the context of monitoring (early) therapeutic intervention, as described in the studies
350 of HD mouse models [10, 33]. Our current work confirmed the *ex vivo* findings that [^{3}H]-
351 radiolabeled CHDI-009R (*Liu et al., under review*) can detect statistically significant phenotypic
352 differences at 3 months of age with both *in vivo* PET imaging and *post-mortem*
353 autoradiography.
354 We have described several mHTT radiotracers that could identify a significant difference in
355 striatal binding in 3-month-old zQ175DN HET mice [11, 17]. Especially [^{11}C]CHDI-180R
356 exhibited high metabolic stability and appropriate brain wash-out for imaging studies in both
357 HD mouse models as well as in a large non-human primate (NHP) model of HD [34],
358 suggesting [^{11}C]CHDI-180R as a well-performing mHTT aggregate-directed PET radioligand
359 for animal models [10, 14]. However, the increased binding potential of [^{3}H]CHDI-009R
360 (B_{max}=448 fmol/mg) compared to [^{3}H]CHDI-180 (B_{max}=163 fmol/mg) in HOM zQ175DN brains
361 likely points towards higher sensitivity to detect mHTT aggregates with CHDI-009R, as shown
362 in postmortem HD brains (*Liu et al., under review*). The utility of [^{3}H]CHDI-009R as an imaging
363 biomarker will be assessed in a clinical setting.
364

365 ## Conclusions

366 [^{11}C]CHDI-009R is a highly stable radioligand capable of detecting significant phenotypic
367 differences between HET and WT zQ175DN mice at different ages in a reproducible manner.
368 These findings suggest [^{11}C]CHDI-009R to be a suitable radioligand to image mHTT
369 aggregates in mice. Notably, a clinical investigation is underway to determine its suitability for
370 assessing mHTT aggregates in humans.
371

Declarations

Ethics approval

Experiments followed the European Committee (decree 2010/63/CEE) and were approved by the Ethical Committee for Animal Testing (ECD 2019–39) at the University of Antwerp (Belgium).

Availability of data and material

The processed data used for the analysis presented in this work will be made available on OpenNeuro upon acceptance of the manuscript for publication.

Acknowledgements

The authors thank Philippe Joye, Caroline Berghmans, Romy Raeymakers and Eleni Van der Hallen of the Molecular Imaging Center Antwerp (MICA) for their valuable assistance. FZ, LE, AVE, JA, AM, JV, SS, and DB are members of the µNeuro Research Centre of Excellence at the University of Antwerp. The authors acknowledge the contribution of the following CHDI staff: Drs Mette Skinbjerg, Robert Doot and Yuchuan Wang for helpful discussions; Drs Simon Noble and Vahri Beaumont for reviewing and providing constructive feedback; Brenda Lager for coordinating animal supply and Braden Boone for project management.

Authors' contributions

Conceptualization: JV, VK, JB, LL, SS, DB

Methodology: JV, AM, SS, DB

Data acquisition: FZ, LE, AVE, SDL

Formal analysis and investigation: FZ, LE, AVE

Data interpretation: FZ, JV, SDL, JA, CD, VK, JB, LL, SS, DB

Writing – original draft preparation: FZ, SS, DB

Writing – review and editing: FZ, LE, JV, SDL, JA, CD, VK, JB, LL, SS, DB

Resources: CD, VK, JB, LL, SS, DB

Funding acquisition: SS, DB

Supervision: JV, SS, DB

Competing interests

This work was funded by CHDI Foundation, Inc., a privately-funded nonprofit biomedical research organization exclusively dedicated to collaboratively developing therapeutics that improve the lives of those affected by Huntington's disease. CD, VK, JB, and LL are employed by CHDI Management, Inc., the company that manages the scientific activities of CHDI Foundation. No other potential conflicts of interest relevant to this article exist.

Funding

This work was funded by CHDI Foundation, Inc. under agreement number A-11627. DB acknowledges support by the Research Foundation Flanders (FWO) (ID: 1229721N). University of Antwerp supported the work through professorships for JV, SS, and DB.

References

1. Saudou, F. and S. Humbert, *The Biology of Huntingtin.* Neuron, 2016. **89**(5): p. 910-26.
2. The-Huntington's-Disease-Collaborative-Research-Group, *A novel gene containing a trinucleotide repeat that is expanded and unstable on Huntington's disease chromosomes.* Cell, 1993. **72**(6): p. 971-983.
3. McColgan, P. and S.J. Tabrizi, *Huntington's disease: a clinical review.* Eur J Neurol, 2018. **25**(1): p. 24-34.
4. Waldvogel, H.J., E.H. Kim, L.J. Tippett, J.P. Vonsattel, and R.L. Faull, *The Neuropathology of Huntington's Disease.* Curr Top Behav Neurosci, 2015. **22**: p. 33-80.
5. Tabrizi, S.J., R. Ghosh, and B.R. Leavitt, *Huntingtin Lowering Strategies for Disease Modification in Huntington's Disease.* Neuron, 2019. **101**(5): p. 801-819.
6. Wild, E.J. and S.J. Tabrizi, *Therapies targeting DNA and RNA in Huntington's disease.* The Lancet Neurology, 2017. **16**(10): p. 837-847.
7. Saade, J. and T.A. Mestre, *Huntington's Disease: Latest Frontiers in Therapeutics.* Curr Neurol Neurosci Rep, 2024. **24**(8): p. 255-264.
8. Caron, N.S., R. Banos, A.E. Aly, Y. Xie, S. Ko, N. Potluri, C. Anderson, H.F. Black, L.M. Anderson, B. Gordon, et al., *Cerebrospinal fluid mutant huntingtin is a biomarker for huntingtin lowering in the striatum of Huntington disease mice.* Neurobiol Dis, 2022. **166**: p. 105652.
9. Kordasiewicz, H.B., L.M. Stanek, E.V. Wancewicz, C. Mazur, M.M. McAlonis, K.A. Pytel, J.W. Artates, A. Weiss, S.H. Cheng, L.S. Shihabuddin, et al., *Sustained therapeutic reversal of Huntington's disease by transient repression of huntingtin synthesis.* Neuron, 2012. **74**(6): p. 1031-44.
10. Bertoglio, D., J. Bard, M. Hessmann, L. Liu, A. Gartner, S. De Lombaerde, B. Huscher, F. Zajicek, A. Miranda, F. Peters, et al., *Development of a ligand for in vivo imaging of mutant huntingtin in Huntington's disease.* Sci Transl Med, 2022. **14**(630): p. eabm3682.
11. Bertoglio, D., J. Verhaeghe, A. Miranda, L. Wyffels, S. Stroobants, L. Mrzljak, V. Khetarpal, M. Skinbjerg, L. Liu, C. Dominguez, et al., *Longitudinal preclinical evaluation of the novel radioligand [11C]CHDI-626 for PET imaging of mutant huntingtin aggregates in Huntington's disease.* Eur J Nucl Med Mol Imaging, 2022. **49**(4): p. 1166-1175.
12. Herrmann, F., M. Hessmann, S. Schaertl, K. Berg-Rosseburg, C.J. Brown, G. Bursow, A. Chiki, A. Ebneth, M. Gehrmann, N. Hoeschen, et al., *Pharmacological characterization of mutant huntingtin aggregate-directed PET imaging tracer candidates.* Sci Rep, 2021. **11**(1): p. 17977.
13. Liu, L., P.D. Johnson, M.E. Prime, V. Khetarpal, M.R. Lee, C.J. Brown, X. Chen, D. Clark-Frew, S. Coe, M. Conlon, et al., *[(11)C]CHDI-626, a PET Tracer Candidate for Imaging Mutant Huntingtin Aggregates with Reduced Binding to AD Pathological Proteins.* J Med Chem, 2021. **64**(16): p. 12003-12021.
14. Bertoglio, D., A.R. Weiss, W. Liguore, L.D. Martin, T. Hobbs, J. Templon, S. Srinivasan, C. Dominguez, I. Munoz-Sanjuan, V. Khetarpal, et al., *In Vivo Cerebral Imaging of Mutant Huntingtin Aggregates Using (11)C-CHDI-180R PET in a Nonhuman Primate Model of Huntington Disease.* J Nucl Med, 2023.
15. Liu, L., M.E. Prime, M.R. Lee, V. Khetarpal, C.J. Brown, P.D. Johnson, P. Miranda-Azpiazu, X. Chen, D. Clark-Frew, S. Coe, et al., *Imaging Mutant*

463 *Huntingtin Aggregates: Development of a Potential PET Ligand.* J Med Chem,
464 2020. **63**(15): p. 8608-8633.
465 16. Liu, L., P.D. Johnson, M.E. Prime, V. Khetarpal, C.J. Brown, L. Anzillotti, D.
466 Bertoglio, X. Chen, S. Coe, R. Davis, et al., *Design and Evaluation of*
467 *[(18)F]CHDI-650 as a Positron Emission Tomography Ligand to Image Mutant*
468 *Huntingtin Aggregates.* J Med Chem, 2022.
469 17. Zajicek, F., J. Verhaeghe, S. De Lombaerde, A. Van Eetveldt, A. Miranda, I.
470 Munoz-Sanjuan, C. Dominguez, V. Khetarpal, J. Bard, L. Liu, et al., *Preclinical*
471 *evaluation of the novel [(18)F]CHDI-650 PET ligand for non-invasive*
472 *quantification of mutant huntingtin aggregates in Huntington's disease.* Eur J
473 Nucl Med Mol Imaging, 2024.
474 18. Delva, A., M. Koole, K. Serdons, G. Bormans, L. Liu, J. Bard, V. Khetarpal, C.
475 Dominguez, I. Munoz-Sanjuan, A. Wood, et al., *Biodistribution and dosimetry*
476 *in human healthy volunteers of the PET radioligands [(11)C]CHDI-00485180-R*
477 *and [(11)C]CHDI-00485626, designed for quantification of cerebral aggregated*
478 *mutant huntingtin.* Eur J Nucl Med Mol Imaging, 2022. **50**(1): p. 48-60.
479 19. Andrew Wood, L.L. *PET ligands Targeting mHTT Aggregates*. 2023 [cited
480 2024 October 16, 2024]; Available from: https://chdifoundation.org/2023-
481 conference/.
482 20. Menalled, L.B., A.E. Kudwa, S. Miller, J. Fitzpatrick, J. Watson-Johnson, N.
483 Keating, M. Ruiz, R. Mushlin, W. Alosio, K. McConnell, et al., *Comprehensive*
484 *behavioral and molecular characterization of a new knock-in mouse model of*
485 *Huntington's disease: zQ175.* PLoS One, 2012. **7**(12): p. e49838.
486 21. Heikkinen, T., K. Lehtimaki, N. Vartiainen, J. Puolivali, S.J. Hendricks, J.R.
487 Glaser, A. Bradaia, K. Wadel, C. Touller, O. Kontkanen, et al., *Characterization*
488 *of neurophysiological and behavioral changes, MRI brain volumetry and 1H*
489 *MRS in zQ175 knock-in mouse model of Huntington's disease.* PLoS One,
490 2012. **7**(12): p. e50717.
491 22. Cudalbu, C., V.A. McLin, H. Lei, J.M. Duarte, A.L. Rougemont, G. Oldani, S.
492 Terraz, C. Toso, and R. Gruetter, *The C57BL/6J mouse exhibits sporadic*
493 *congenital portosystemic shunts.* PLoS One, 2013. **8**(7): p. e69782.
494 23. Bertoglio, D., J. Verhaeghe, A. Miranda, I. Kertesz, K. Cybulska, S. Korat, L.
495 Wyffels, S. Stroobants, L. Mrzljak, C. Dominguez, et al., *Validation and*
496 *noninvasive kinetic modeling of [(11)C]UCB-J PET imaging in mice.* J Cereb
497 Blood Flow Metab, 2020. **40**(6): p. 1351-1362.
498 24. Miranda, A., D. Bertoglio, D. Glorie, S. Stroobants, S. Staelens, and J.
499 Verhaeghe, *Validation of a spatially variant resolution model for small animal*
500 *brain PET studies.* Biomed Phys Eng Express, 2020. **6**(4): p. 045001.
501 25. Bertoglio, D., J. Verhaeghe, L. Kosten, D. Thomae, A. Van der Linden, S.
502 Stroobants, J. Wityak, C. Dominguez, L. Mrzljak, and S. Staelens, *MR-based*
503 *spatial normalization improves [18F]MNI-659 PET regional quantification and*
504 *detectability of disease effect in the Q175 mouse model of Huntington's*
505 *disease.* PLoS One, 2018. **13**(10): p. e0206613.
506 26. Johnson, G.A., A. Badea, J. Brandenburg, G. Cofer, B. Fubara, S. Liu, and J.
507 Nissanov, *Waxholm space: an image-based reference for coordinating mouse*
508 *brain research.* Neuroimage, 2010. **53**(2): p. 365-72.
509 27. Bertoglio, D., J. Verhaeghe, S. Korat, A. Miranda, L. Wyffels, S. Stroobants, L.
510 Mrzljak, C. Dominguez, L. Liu, M. Skinbjerg, et al., *In vitro and In vivo*
511 *Assessment of Suitable Reference Region and Kinetic Modelling for the*

mGluR1 Radioligand [(11)C]ITDM in Mice. Mol Imaging Biol, 2020. **22**(4): p. 854-863.

28. Bertoglio, D., F. Zajicek, S. Lombaerde, A. Miranda, S. Stroobants, Y. Wang, C. Dominguez, I. Munoz-Sanjuan, J. Bard, L. Liu, et al., *Validation, kinetic modeling, and test-retest reproducibility of [(18)F]SynVesT-1 for PET imaging of synaptic vesicle glycoprotein 2A in mice.* J Cereb Blood Flow Metab, 2022. **42**(10): p. 1867-1878.
29. Verhaeghe, J., D. Bertoglio, L. Kosten, D. Thomae, M. Verhoye, A. Van Der Linden, L. Wyffels, S. Stroobants, J. Wityak, C. Dominguez, et al., *Noninvasive Relative Quantification of [(11)C]ABP688 PET Imaging in Mice Versus an Input Function Measured Over an Arteriovenous Shunt.* Front Neurol, 2018. **9**: p. 516.
30. G., P. and F. K., *The mouse brain in stereotaxic coordinates: Academic Press*. 2 edition ed. 2003.
31. Cassinelli Petersen, G., M. Roytman, G.C. Chiang, Y. Li, M.L. Gordon, and A.M. Franceschi, *Overview of tau PET molecular imaging.* Curr Opin Neurol, 2022. **35**(2): p. 230-239.
32. Cicchetti, D., *Guidlines, Criteria, and Rules of Thum for Evaluating Nomred and Standardized Assessment Instruments in Psychology.* Psychological Assessment, 1994. **6**(4): p. 284-290.
33. Marchionini, D.M., S. De Lombaerde, J. van Rijswijk, F. Zajicek, L. Everix, A. Miranda, M.J. Aaltonen, C.M. Kluger, T. Wild, A. Kakoulidou, et al., *Pharmacodynamic biomarkers responsive to mutant huntingtin lowering in a Huntington's disease mouse model.* Neurobiol Dis, 2025. **209**: p. 106906.
34. Weiss, A.R., W.A. Liguore, K. Brandon, X. Wang, Z. Liu, J.S. Domire, D. Button, S. Srinivasan, C.D. Kroenke, and J.L. McBride, *A novel rhesus macaque model of Huntington's disease recapitulates key neuropathological changes along with motor and cognitive decline.* Elife, 2022. **11**.

542 # Tables

543 ***Table 1 [^{11}C]CHDI-009R $V_{T\ (IDIF)}$ (Logan) [mL/cm^3] quantitative values in 9-month-old mice***

544

	WT (mean±SD)	HET (mean±SD)	*Post-hoc p* value	Δ±SE [%]
Striatum	0.46±0.05	0.90±0.11	<0.0001	94.6±6.2
Motor Cortex	0.47±0.06	0.88±0.13	<0.0001	88.8±6.3
Hippocampus	0.45±0.04	0.83±0.11	<0.0001	85.9±6.4
Thalamus	0.46±0.05	0.94±0.13	<0.0001	105.8±6.2
Cerebellum	0.52±0.06	0.81±0.10	<0.0001	55.5±5.4

545
546
547
548

549 WT: *n*=20; HET: *n*=19. SD = standard deviation; Δ = phenotypic difference; SE = standard error

550

551 ***Table 2 [^{11}C]CHDI-009R test-retest $V_{T\ (IDIF)}$ values and relative and absolute test-retest***

552 ***variability in 9-month-old mice***

	Test $V_{T\ (IDIF)}$ (Logan) [mL/cm^3]		Retest $V_{T\ (IDIF)}$ (Logan) [mL/cm^3]		rTRV [%]		aTRV [%]		ICC
	WT	**HET**	**WT**	**HET**	**WT**	**HET**	**WT**	**HET**	
Striatum	0.45±0.04	0.84±0.06	0.46±0.04	0.82±0.10	-0.9±6.7	0.9±9.2	5.1±4.0	7.7±4.2	0.62
Motor Cortex	0.49±0.04	0.79±0.07	0.47±0.03	0.84±0.12	4.3±8.3	-4.8±6.2	7.0±5.8	6.3± 4.5	0.79
Hippocampus	0.43±0.04	0.77±0.06	0.44±0.04	0.66±0.04	-1.8± 7.4	1.2 ± 8.3	6.1± 4.2	6.9± 4.1	0.71
Thalamus	0.44±0.03	0.84±0.07	0.46±0.04	0.81±0.08	-3.1±8.5	-0.1±7.8	6.2± 6.2	5.2±5.4	0.72
Cerebellum	0.49±0.04	0.72±0.05	0.50±0.05	0.67±0.04	-2.1± 8.3	-0.1± 8.0	6.2± 5.5	6.3± 4.2	0.63

553

554 *rTRV = relative test-retest variability; aTRV = absolute test-retest variability; ICC = Intraclass*

555 *correlation coefficient. Data is given as mean±SD. WT: n=8; HET: n=8*

556

557 ***Table 3 [^{11}C]CHDI-009R $V_{T\ (IDIF)}$* (Logan) [mL/cm^3] *quantitative values in 3-month-old mice***

558
559
560
561
562
563

	WT (mean±SD)	HET (mean±SD)	*Post hoc* *p* value	Δ±SE [%]
Striatum	0.46±0.03	0.52±0.04	0.0002	12.3±2.9
Motor Cortex	0.47±0.04	0.50±0.06	0.3989	5.0±2.8
Hippocampus	0.44±0.03	0.48±0.04	0.0194	8.9±3.0
Thalamus	0.46±0.03	0.53±0.05	<0.0001	16.3±2.9
Cerebellum	0.50±0.03	0.54±0.04	0.0104	8.3±2.7

564 *WT: n=18; HET: n=19. SD = standard deviation; Δ = phenotypic difference; SE = standard error*

565

566 **Figures**

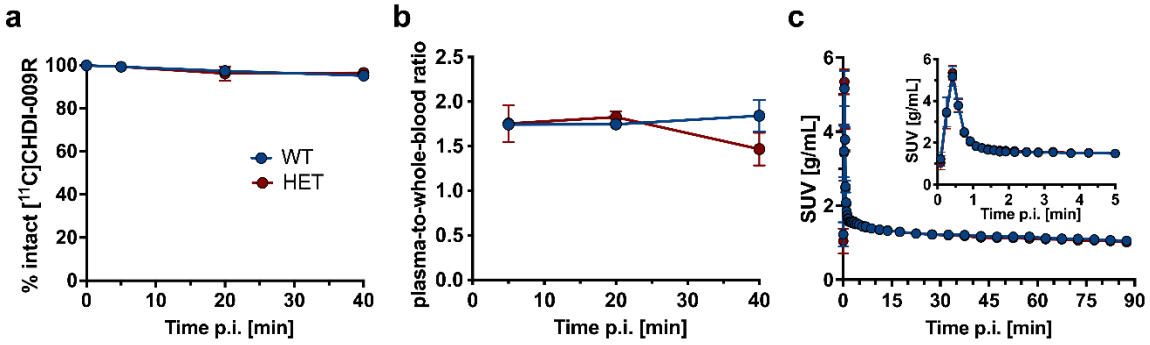

567

568 ***Fig. 1*** *[^{11}C]CHDI-009R plasma analysis and IDIF of WT and HET zQ175DN mice. a, The intact*
569 *radioligand in percentage for plasma over time. b, Plasma-to-whole-blood ratio over time in both*
570 *genotypes. c, Averaged IDIF SUV curves over 90 min scan time for both genotypes. c: Data are*
571 *represented as mean±SEM. a and b: n=2-5 per genotype and timepoint; c: WT: n=20; HET: n=19*

572

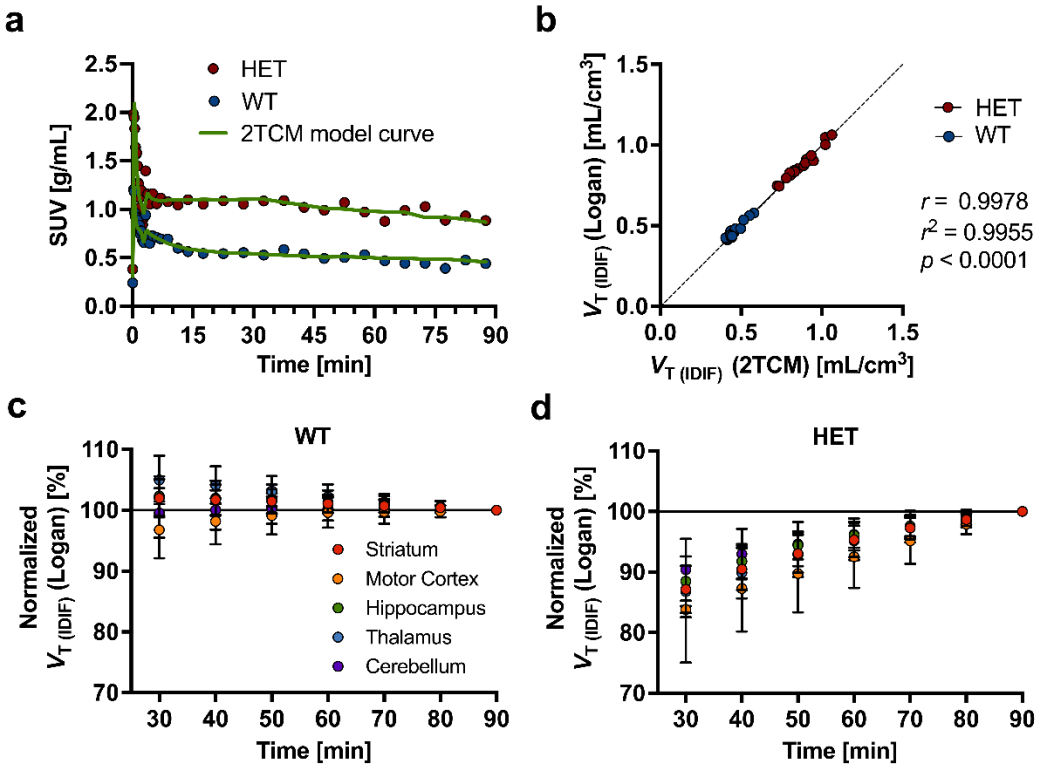

573

574 ***Fig. 2*** *[^{11}C]CHDI-009R brain kinetic modeling and $V_{T\ (IDIF)}$ time stability with Logan. a, Exemplary*
575 *striatal SUV TAC curves of WT and HET animals fitted to 2TCM. b, Pearson's correlation of striatal*
576 *$V_{T\ (IDIF)}$ values with 2TCM and Logan for verification with simple linear regression. $V_{T\ (IDIF)}$ time*
577 *stability of Logan in WT (c) and HET (d) mice. $V_{T\ (IDIF)}$ values were normalized to the 90 min scan*
578 *acquisition time. b-d: WT: n=20; HET: n=19*

579

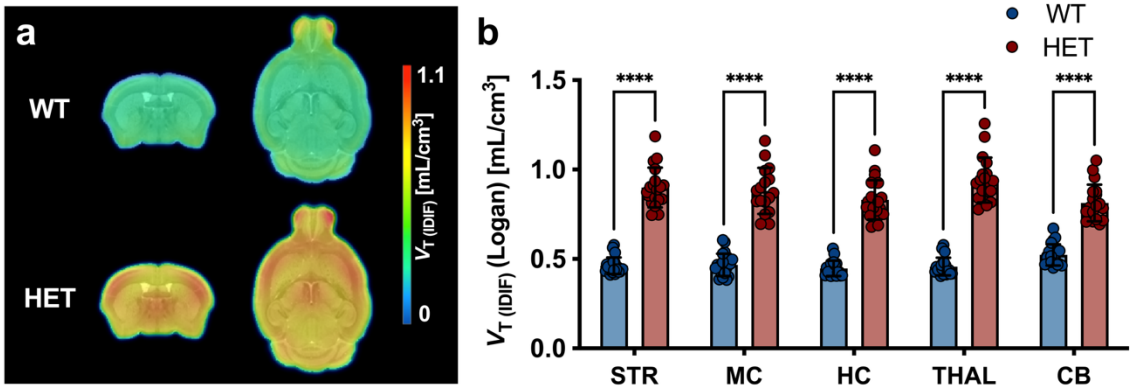

580

581 ***Fig. 3*** *[^{11}C]CHDI-009R mHTT aggregate quantification in 9-month-old mice. a, Group-averaged*
582 *parametric maps for WT and HET zQ175DN mice overlaid onto MRI template. b, [^{11}C]CHDI-009R*
583 *$V_{T\ (IDIF)}$ estimations in WT and HET mice. Two-way ANOVA with post-hoc Bonferroni for multiple*
584 *comparisons. ****p<0.0001. WT: n=20; HET: n=19. STR = Striatum; MC = Motor Cortex; HC =*
585 *Hippocampus; THAL = Thalamus; CB = Cerebellum*

586

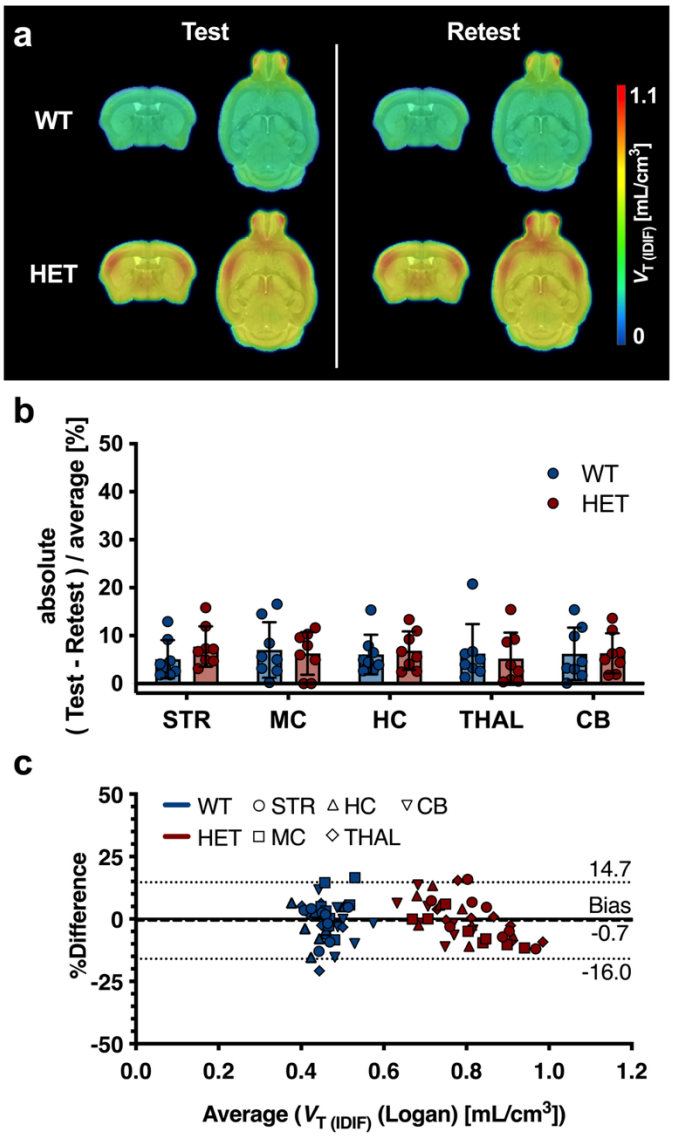

587

588 ***Fig. 4*** *[^{11}C]CHDI-009R test-retest variability analysis in 9-month-old mice. a, Group-averaged*
589 *parametric maps for WT and HET zQ175DN mice at test and retest overlaid onto MRI template.*
590 *b, Absolute test-retest variability analysis in percentage. c, Bland-Altman plot to display the level*
591 *of agreement between test and retest. WT: n=8; HET: n=8. STR = Striatum; MC = Motor Cortex;*
592 *HC = Hippocampus; THAL = Thalamus; CB = Cerebellum*

593

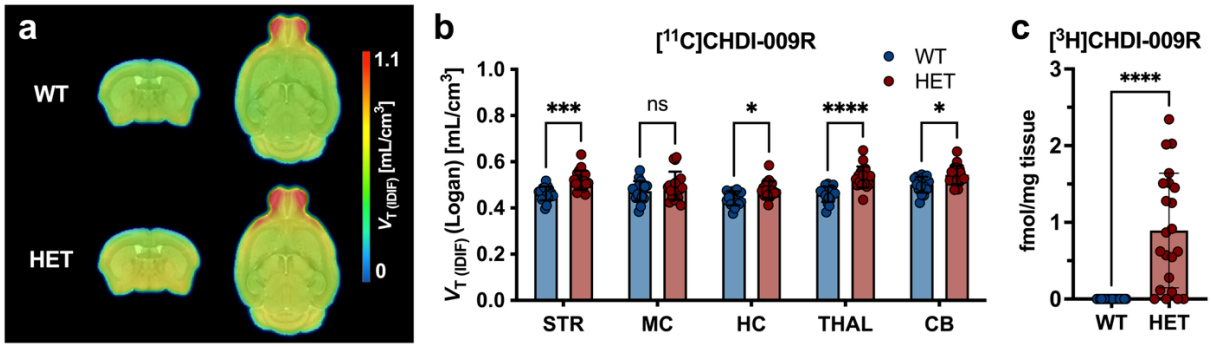

Fig. 5 *mHTT quantification in 3-month-old mice. a, Group-averaged parametric maps for WT and HET zQ175DN mice overlaid onto MRI template. b, [^{11}C]CHDI-009R $V_{T\ (IDIF)}$ estimations in WT and HET mice. c, [^{3}H]CHDI-009R autoradiography of the whole brain in the same mice. ns=not significant; * p<0.05; *** p<0.001; **** p<0.0001. a and b: WT: n=18; HET: n=19; c: WT: n=14; HET: n=20. STR = Striatum; MC = Motor Cortex; HC = Hippocampus; THAL = Thalamus; CB = Cerebellum*

602 **Supplemental information**

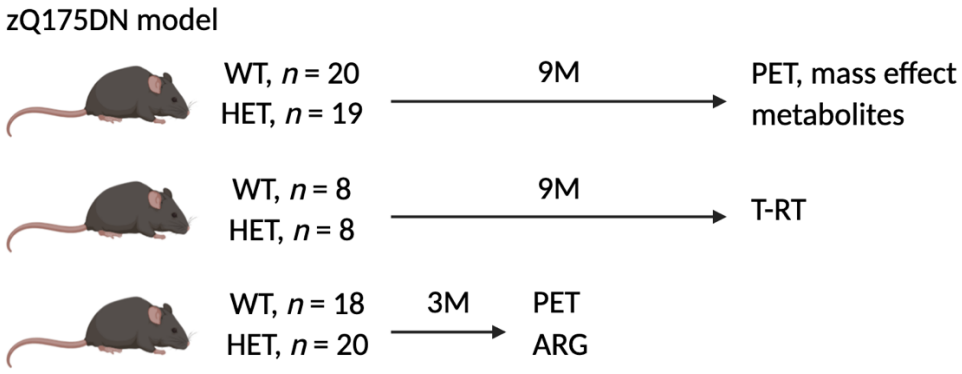

603

604 ***Fig. S1 Overview of the experimental design.*** *Number and age of each experimental group for*
605 *the different experimental setups. n = number; M = months; PET = dynamic PET scans;*
606 *metabolites = metabolite analysis; T-RT = test-retest; ARG = Autoradiography*

607

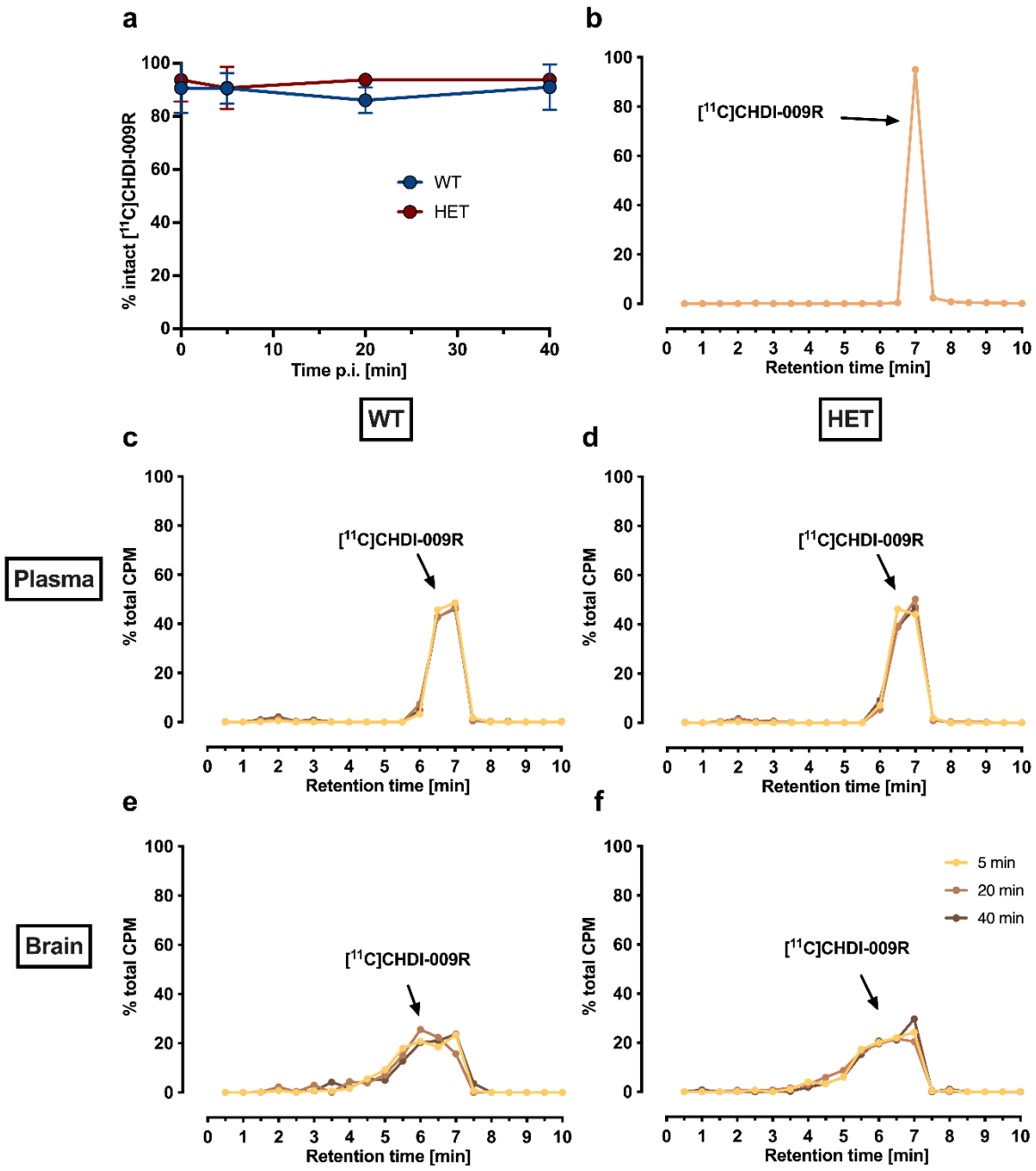

Fig. S2 [^{11}C]CHDI-009R metabolite analysis in WT and HET zQ175DN mice. *a, Intact radioligand in percentage for brain over time in both genotypes. b, Decay-corrected reconstructed radiochromatogram for the pure tracer. Decay-corrected reconstructed radiochromatograms for all time points in plasma (c and d) and brain (e and f) for WT (c and e) and HET mice (d and f). Data is given as mean±SD (a) or mean (b-f). n=2-3 per time point and genotype*

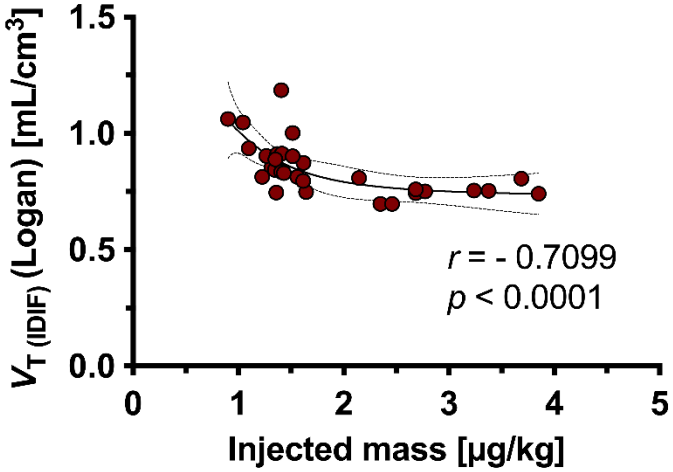

615

616 ***Fig. S3 Mass dose effect in striatum of HET zQ175DN mice at 9 months.*** *Spearman's*
617 *correlation of injected masses (µg/kg) and striatal Logan $V_{T\ (IDIF)}$ values. The sigmoidal interpolation*
618 *(sigmoidal, 4PL, X is concentration) estimates the influence of higher injected masses on the*
619 *$V_{T\ (IDIF)}$ value. The upper mass dose limit was recommended to be 1.7µg/kg. Data is represented*
620 *as individual points. n=30*

621

622 ***Table S1 Scan parameters during the PET imaging study in WT and HET zQ175DN mice***

623 ***for the test-retest study***

	Test	Retest		Test	Retest	
	WT (*n* = 8)		***p* value**	**HET (*n* = 8)**		***p* value**
Injected activity (MBq)	6.3±1.6	7.1±2.5	0.1507	5.3±1.7	5.7±2.2	0.5148
A_M (GBq/µmol) at EOS	112.6±28.6	122.8±26.9	0.3682	107.9±30.6	111.2±24.8	0.9375
Weight (g)	34.8±3.4	33.9±2.8	0.0006	30.8±2.6	30.1±2.2	0.0023
Age (d)	257.5±7.5	261.0±10.4	<0.0001	261.1±9.5	267.0±13.9	0.0143
Injected mass (µg/kg)	1.31±0.15	1.27±0.17	0.6242	1.27±0.14	1.22±0.14	0.9275

624

625 Data is given as mean±SD. Unpaired t-test for comparison of genotypes. A_M = molar activity;

626 EOS = end of synthesis

627

628 ***Table S2 Animal and dose parameters for the PET imaging study in WT and HET zQ175DN***

629 ***mice for the evaluation at 9 months***

630
631
632
633
634
635
636

	WT (*n* = 20)	HET (*n* = 19)	*p* value
Injected activity (MBq)	3.8±0.6	4.5 ± 1.2	0.0062
A_M (GBq/µmol) at EOS	71.2±16.1	73.2 ± 16.8	0.7122
Weight (g)	29.7±1.8	34.8 ± 2.8	<0.0001
Age (d)	263.3±4.3	263.2 ± 2.7	0.9221
Injected mass (µg/kg)	1.38 ± 0.20	1.35 ± 0.28	0.9337

637 Data is given as mean±SD unless stated otherwise. Unpaired t-test for comparison of genotypes.

638 A_M = molar activity; EOS = end of synthesis

639

640 ***Table S3 Animal and dose parameters for the PET imaging study in WT and HET zQ175DN***

641 ***mice for the evaluation at 3 months***

642

643

644

645

646

647

	WT (*n* = 18)	HET (*n* = 19)	*p* value
Injected activity (MBq)	5.0±0.9	4.8±0.9	0.4608
A_M (GBq/µmol) at EOS	100.8±16.6	99.1±17.9	0.7676
Weight (g)	28.4±2.2	27.7±1.8	0.2975
Age (d)	108.0±3.3	106.6±4.1	0.2523
Injected mass (µg/kg)	1.31 ± 0.14	1.34 ± 0.19	0.6164

648 Data is given as mean±SD. Unpaired t-test for comparison of genotypes. A_M = molar activity;

649 EOS = end of synthesis

650

651 ***Table S4 [^{11}C]CHDI-009R power analysis of 3- and 9-month-old mice***

age [M]	Brain region	striatal Δ±SE [%]	Cohen's *d*	10%	20%	30%	40%	50%	100%
3	**Striatum**	12.3±2.9	1.70	551	139	62	36	23	6
	Motor Cortex	5.0±2.8	0.59	4947	1238	540	310	199	37
	Hippocampus	8.9±3.0	1.13	1238	310	136	78	51	11
	Thalamus	16.3±2.9	1.70	632	159	70	41	26	6
	Cerebellum	8.3±2.7	1.13	1238	310	136	78	51	11
9	**Striatum**	95.8±6.1	5.15	78	21	10	6	4	2
	Motor Cortex	88.8±6.3	4.05	125	32	15	9	6	2
	Hippocampus	85.9±6.4	4.59	105	27	13	8	5	2
	Thalamus	105.8±6.2	4.87	92	24	11	7	5	2
	Cerebellum	55.5±5.4	3.52	148	38	17	10	7	3

652

653 *One-tailed power analysis with α=0.05 and β=80%. Animal numbers needed for significance*

654 *between treated and non-treated HET groups in a mHTT-lowering study. 100% equals difference*

655 *between non-treated HET and WT groups. 3 months: WT: n=18; HET: n=19; 9 months: WT:*

656 *n=20; HET: n=19. M = months; Δ = phenotypic difference; SE = standard error*

657